Ballistic impact of layered and case-hardened steel plates

Jens Kristian Holmen[a,b,*], Jan Ketil Solberg[c], Odd Sture Hopperstad[a,b], Tore Børvik[a,b]

[a]*Structural Impact Laboratory (SIMLab), Department of Structural Engineering, NTNU, Norwegian University of Science and Technology, Trondheim, Norway.*

[b]*Centre for Advanced Structural Analysis (CASA), NTNU, Trondheim, Norway.*

[c]*Department of Materials Science and Engineering, NTNU, Trondheim, Norway.*

Abstract

We investigated the ballistic resistance of hot-rolled structural steel plates with a nominal yield stress of 355 MPa in this study. Ballistic tests were conducted with 7.62 mm armor piercing bullets on monolithic and multi-layered configurations both in the as-received (AR) state and in a case-hardened (CH) state. In the CH state we made the surface stronger while preserving a relatively ductile core. This was done to improve the ballistic properties of the plates. Quasi-static uniaxial tension tests and Vickers hardness tests were conducted to calibrate constitutive models for numerical simulations. The ballistic tests revealed that the capacity was highest for a monolithic CH plate, and that case hardening increased the perforation resistance by more than 20%. Plate layering decreased the capacity of the CH plates, while the capacity of the AR plates did not decrease consistently by increasing the number of layers. Finally, we used the hardness measurements to distribute material properties across the thickness of the CH plates. These distributed material properties were used in numerical models. Finite element simulations gave predominantly conservative results within 11% of the experimental values.

Keywords*: Penetration, Structural steel, Node splitting, Laminated plates, Small-arms bullets*

[*]Corresponding author (URL: http://www.ntnu.edu/casa)
E-mail address: jens.k.holmen@ntnu.no

1 Introduction

The perforation resistance of multi-layered plates compared to that of monolithic plates has been a subject of research, and of controversy, for a long time [1][2]. Numerous parameters affect the ballistic capacity of layered plates, e.g., impact velocity, material strength and ductility, target-plate span, spacing and thickness, and also the order of the plates if they are made of dissimilar materials or have different thicknesses. The existing literature contains studies of multi-layered plates with various combinations of the parameters mentioned above. Since lamination might simplify manufacturing, transportation and assembly of protective solutions, the main objectives of these studies were to either improve the design of protective structures, or to determine the gain or loss in capacity by using multi-layered configurations.

More specifically, Marom and Bodner [3] found that layering might be beneficial to resist perforation by round, relatively soft, lead bullets. Corran et al. [4] later saw that multi-layered targets performed better than monolithic targets when the target plates were above 4-6 mm thick. Further, they highlighted that the effect of layering is extremely dependent upon the projectile-nose shape and hardness as well as the impact velocity. The effect of nose shape was exemplified by investigations of sub-ordnance velocity impacts by Dey et al. [5]. Double-layered (2×6 mm) steel target plates performed much better than one 12 mm thick plate against a blunt-nosed projectile, whereas the monolithic configuration had a higher capacity against perforation by ogival-nosed projectiles of the same weight (see also Teng et al. [1][6]). In contrast, when thin plates were subjected to impacts at low velocities the ballistic capacity was reduced with layering for both nose shapes [7], but more for ogival than for blunt-nosed impactors. Little, or negative, effect of layering was found by Gupta and Madhu [8], Gupta et al. [9], Iqbal et al. [10], and Iqbal and Gupta [11]. Other studies also highlight the complexity of the problem, see e.g., Refs. [12][13][14][15]. Recently, Ben-Dor et al. [2] presented a state-

of-the-art review of optimization of multi-layered configurations and concluded that perforation mechanism and velocity regime strongly affect the ballistic capacity.

Børvik et al. [16] and Holmen et al. [17] reported that material strength is the most important parameter for perforation resistance, but if the local ductility is not sufficient to prevent fragmentation, the ballistic limit velocity can actually decrease with increasing strength [18]. Surface strengthening of relatively weak and ductile steel plates can in theory increase the material strength while preserving the ductility. Lou et al. [19] conducted an experimental study on ballistic perforation of surface strengthened steel plates and found that the ballistic limit velocity increased significantly after the surface-strengthening procedure. The main focus of that study was not, however, the ballistic perforation, but the metallurgical aspects of the procedure also known as case hardening.

Case hardening is a manufacturing process commonly used to obtain a hard and durable outer surface and a ductile inner core of for instance screws, bolts, nuts, gears, lock shackles, and agricultural equipment. Steels with 0.13-0.20% carbon and a ferrite/pearlite structure can be carburized by placing the specimen in a carbon-rich environment at a temperature between 850 °C and 950 °C. At this elevated temperature, the steel transforms into an austenite structure that can contain more carbon than the initial structure leading to diffusion of carbon atoms into the surface of the specimen. After cooling, we get a coarse martensitic structure that can be refined by subsequent heat treatment. Tempering usually takes place at the end of the process to alleviate the internal stresses. Depending on the details of the heat treatment a martensitic surface with a ferritic or a martensitic core is obtained [20][21].

The experimental objectives of this study are to investigate how the capacity of multi-layered target plates compare to monolithic targets of the same total thickness, and to compare the performance of case-hardened plates to plates in the as-received state. We present ballistic limit velocities resulting from numerous impacts by 7.62 mm armor piercing bullets together

with uniaxial tension and Vickers hardness tests. Constitutive and failure models were calibrated from these material tests. In the numerical part of the paper, the predictive capability of finite element simulations employing node splitting was evaluated against the experimental results.

The variation of material properties across the thickness of the plates resulting from the case-hardening procedure was included in the finite element models. We present, in the paper, a method that scales the initial yield stress in the constitutive model as a function of Vickers hardness, effectively taking into account this variation. The method assumes proportionality between the Vickers hardness and the ultimate engineering tensile stress (UTS).

Since case hardening makes the surface of the steel plates less ductile than the core, we used node splitting in an attempt to simulate the resulting quasi-ductile perforation mechanisms seen in the impact tests. Node splitting is an alternative to element erosion for introducing fracture into a finite element model. It has received some attention in the past, specifically for two-dimensional problems [22][23][24]. In this study we used a general three-dimensional formulation that is available in the IMPETUS Afea Solver [25] which has formerly been applied by for instance Holmen et al. [18], Ruggiero et al. [26] and Olovsson et al. [27]. Advantages of node splitting are that failure does not imply removal of an element meaning that mass and energy loss can be reduced compared to element erosion, and that fragmentation can be captured due to the explicit modeling of crack growth. However, studies employing node splitting are still rare and further assessment of the method applied in structural impact analysis is definitely needed.

2 Materials

2.1 NVE 36 steel plates

NVE 36 is a structural steel with a carbon content of 0.15 wt.-% and nominal yield stress of 355 MPa (designated S355J according to the European standard (EN)). Its intended

applications are in maritime structural components. This study considers hot-rolled plates with in-plane dimensions 300 mm × 300 mm and three different thicknesses: 12 mm, 6 mm, and 4 mm in either a monolithic configuration (1×12 mm) or laminated configurations (2×6 mm and 3×4 mm). Table 1 shows the complete chemical composition of the steel. Some plates were tested in the as-received (AR) condition and some plates were case hardened (CH) before testing, meaning that they were kept in a carbon-rich environment at elevated temperatures to increase the surface strength while keeping the core relatively unchanged.

The case-hardening procedure was based on a series of previously conducted experimental studies (e.g., Ref. [28]). It started by subjecting the plates to carburization in a pit furnace at 920 °C for 4 h for the 4 mm thick plates, and 6 h for the 6 mm and 12 mm plates before air cooling back to room temperature. They were then reheated to 920 °C for a shorter time-period, where precautions were taken to ensure that the plates were hot through the entire thickness for at least 10 min before they were quenched in a 10% NaOH solution. Lastly, all the plates were tempered at 245 °C for 2 h.

2.2 Material testing

We conducted two types of material tests: quasi-static uniaxial tension tests and Vickers hardness tests. Tension testing was done on specimens extracted from the core of the 12 mm AR and CH plates while every plate in both conditions were subjected to Vickers hardness testing.

Cylindrical specimens were machined in the rolling direction of the plate and used in the tension testing (see e.g., Ref. [17] for the geometry). The nominal diameter of the 40 mm gauge section was 6 mm and the cross-bar velocity during testing was 1.2 mm/min, giving an initial strain rate of 5.0×10^{-4} s^{-1}. A calibrated load cell recorded the force F, while a laser-scan micrometer placed on a moving frame continuously measured the minimum diameter in two perpendicular directions all the way to fracture. Figure 1 presents the average true stress σ_t as

a function of the plastic strain ε^p from representative tests. These quantities were calculated as

$$A = \frac{\pi}{4} D_z D_\perp, \qquad \sigma_t = \frac{F}{A}, \qquad \varepsilon^p = \varepsilon - \varepsilon^e = \ln\left(\frac{A_0}{A}\right) - \frac{\sigma_t}{E} \tag{1}$$

where ε is the average logarithmic strain, ε^e is the elastic strain, $E = 210\,000$ MPa is the Young's modulus, A_0 is the initial area, and A is the current minimum area of the specimen's cross section, while D_z and $D_\perp$ are the minimum diameters in the thickness and transverse directions of the plate, respectively. We assume a Poisson's ratio ν of 0.33 in this study.

The hardness distributions across the thickness of the plates are shown in Figure 2. A 0.2 kg diamond-shaped indenter was pressed against the material surface and held constant for 15 s. Vickers hardness (HV) is defined as the load divided by the surface area of the indentation [21]. Indentation paths were made on a sample approximately 15 mm from the edge of a penetration channel. We left 80 μm between each indent near the surface, but the indentation interval was increased near the center of the sample. By inspecting Figure 2, we find that case hardening strengthened the entire thickness of the plate due to rapid cooling of the whole cross section, but the surface regions more than the core. The hardness profiles for the two 6 mm plates are different (Figure 2b) due to a mistake that was done during the processing of the softest of the two plates, but this difference is of minor importance in the present study.

The micrograph in Figure 3a confirms that the 12 mm thick NVE 36 plates in the AR state consists of ferrite (light gray) and pearlite (black). Figure 3b and c, respectively, show the microstructure in the core and at the surface of the 12 mm thick CH plate. Martensite is the dominating microstructure in both positions. In general, martensite decreases the ductility of steels, but increases their hardness [29][30].

3 Ballistic testing

3.1 Test program

A smooth-bored Mauser rifle was used to fire 7.62 mm armor piercing (AP) bullets toward the target plates. The bullets had a total mass of about 10.5 g including an ogival-shaped hardened steel core of about 5.0 g, a brass jacket, and a lead cap (Figure 4). The distance between the muzzle and the target was 1 m and the rifle was mounted in a rigid rack and fired from a safe distance by a magnetic trigger. Varying the amount of powder in the cartridge meant that we could predetermine the striking velocity with an accuracy of ± 20 m/s. A Phantom v1610 high-speed camera operating at 75,000 fps recorded the penetration event and these camera recordings were used to optically measure the exact striking and residual velocities of the bullet. Figure 5 shows some images of the perforation process from selected impact tests.

The objective of the ballistic testing was to determine the ballistic limit velocities of the various target configurations. Six configurations were tested: 12 mm, 2×6 mm, and 3×4 mm plates both in the AR and CH conditions. Neither of the 300 mm × 300 mm plates suffered more than nine impacts. Striking velocities ranged from 450 m/s to 915 m/s for configurations in the AR state and from 680 m/s to 915 m/s for configurations in the CH state. We conducted a total of 57 successful impact tests.

3.2 Test results

Figure 6a shows the residual velocities from all the ballistic impact tests plotted as a function of striking velocity. The ballistic limit velocities and the residual versus initial velocity curves were found from a best fit of the generalized Recht-Ipson model [31], also known as the Lambert-Jonas equation [32], to the experimental data. The equation reads

$$v_{\mathrm{r}} = a\left(v_{\mathrm{i}}^{p} - v_{\mathrm{bl}}^{p}\right)^{1/p} \tag{2}$$

where v_r is the residual velocity, v_i is the initial/striking velocity, and v_{bl} is the ballistic limit velocity; a and p are model parameters controlling the shape of the ballistic limit curve. Table 2 summarizes the ballistic limit velocities and the fitted model parameters.

3.3 Discussion of test results

We find that the case hardening procedure had a pronounced effect on the perforation resistance of the plates (Figure 6a and Figure 7). The ballistic limit velocity of the CH condition increased by more than 20 % from the AR condition, regardless of layering. This was as expected since the average strength and hardness of the CH plates are considerably higher.

We cannot draw definite conclusions with regards to the effects of layering based on the limited data from this study. However, it appears that the ballistic limit velocity does not increase with increasing number of layers for this nose shape, indicating that lamination is not beneficial for the ballistic capacity against ogival-nosed projectiles in this velocity regime. The CH condition seems to be sensitive to lamination, and even though the average hardness across the thickness of the laminated target configurations is higher than for the monolithic plate we observe a drop of the ballistic limit velocity of almost 5 % from a 12 mm plate to 3×4 mm plate. Our results regarding the lamination of AR plates are inconclusive, but it appears that the ballistic limit velocity does not significantly depend upon the lamination configuration for this condition.

It seems that the extent of global deformation and amount of fragmentation can help explain the ballistic results. AR plates exhibited nearly perfect ductile behavior as described by Backman and Goldsmith [33]. Ductile hole growth was the dominating perforation mechanism (Figure 8a), but limited petaling was seen on the rear side of some of the plates. A distinct dish could also be identified. The dish grew larger and reached farther from the impact area for increasing number of layers (thinner plates) which might have counteracted the drop in perforation resistance that is expected for laminated plates struck by bullets with this nose

shape (see e.g., [5]). Contrary to the ductile behavior of the AR plates, the CH plates displayed almost no dishing. The total thickness of ductile material decreases with increasing number of layers (Figure 2), and low ductility promotes fragmentation. Fragmentation could, along with severe petaling, be identified in several of the tests (Figure 8b). These differences in perforation mechanisms might explain why the CH state is more sensitive to layering than the AR state.

Extrapolating the results from this study must be done with caution. The projectile nose shape and size influence the effect of layering. For instance, Dey et al. [5] found that the ballistic limit velocity of a laminated target was lower than that of a monolithic target when they were subjected to impact by 20 mm ogival-nosed projectiles. Laminated targets were on the other hand advantageous when the impacting projectile had a blunt nose. Flores-Johnson et al. [14] concluded that monolithic plates struck by 7.62 mm AP bullets have slightly better ballistic performance than laminated plates made of the same material, but their material (Weldox 700 E) had significantly higher strength than as-received NVE 36 [14][16].

4 Numerical simulations

4.1 Material modeling

In this work we used a modified version of the Johnson-Cook material model [34][35]. The equivalent stress $\sigma_{\text{eq}} = \sqrt{\frac{3}{2}\sigma'_{ij}\sigma'_{ij}}$, σ'_{ij} being the stress deviator, is a function of the quasi-static flow stress, the strain rate, and temperature:

$$\sigma_{\text{eq}} = \left(A + \sum_{i=1}^{2} Q_i \left(1 - \exp\left(-C_i p\right)\right)\right)\left(1 + \frac{\dot{}}{\dot{}}\right)^{c}\left(1 - \left(\frac{T - T_{\text{r}}}{T_{\text{m}} - T_{\text{r}}}\right)^{m}\right). \quad (3)$$

A is the initial yield stress, Q_i and C_i are hardening parameters, p and $\dot{}$ are the equivalent plastic strain and strain rate, respectively, $\dot{}$ is a reference strain rate chosen as the initial strain rate in the tension tests, and c is the exponent controlling the rate sensitivity of the material. Temperature softening is governed by the exponent m, while T is the current

temperature, T_r is the ambient temperature, and T_m is the melting temperature of the material. In this study, $T_\mathrm{r} = 293\,\mathrm{K}$ and we assumed a melting temperature of $T_\mathrm{m} = 1800\,\mathrm{K}$. Assuming adiabatic conditions, the temperature was calculated as

$$T = T_r + \int_0^p \frac{\chi}{\rho C_\mathrm{p}} \sigma_\mathrm{eq} \mathrm{d}p\,, \tag{4}$$

where ρ is the density, C_p is the specific heat, and $\chi = 0.9$ is the Taylor-Quinney coefficient representing the proportion of plastic work that is converted into heat.

We employed the uncoupled, one-parameter criterion of Cockcroft and Latham (CL) to model failure [36]. It reads

$$D = \frac{1}{W_\mathrm{cr}} \int_0^p \langle \sigma_1 \rangle \mathrm{d}p, \qquad \langle \sigma_1 \rangle = \max(\sigma_1, 0)\,, \tag{5}$$

where D is the damage parameter, W_cr is the CL failure parameter, and σ_1 is the major principal stress. According to Eq. (5) damage grows only when tensile stresses are present. A single uniaxial tension test is sufficient to find W_cr, and thus to calibrate the CL criterion. In the numerical simulations failure occurs when D reaches the value 1.0 in an integration point.

The CL criterion implicitly accounts for the pressure and the third invariant of the deviatoric stress tensor through the major principal stress:

$$\sigma_1 = \left(\sigma^* + \frac{3 - L}{3\sqrt{3 + L^2}} \right) \sigma_\mathrm{eq}\,. \tag{6}$$

Here $\sigma^* = (\sigma_1 + \sigma_2 + \sigma_3)/(3\sigma_\mathrm{eq})$ is the stress triaxiality ratio and $L = (2\sigma_2 - \sigma_1 - \sigma_3)/(\sigma_1 - \sigma_3)$ is the Lode parameter, where $\sigma_1 \geq \sigma_2 \geq \sigma_3$ are the ordered principal stresses. It transpires from Eqs. (5) and (6) that the damage evolution is driven by the plastic power, but amplified by a factor that accounts for the stress state. Figure 9a shows the failure locus for the AR plates at quasi-static strain rate and room temperature, and it appears that the failure strain decreases as the stress triaxiality ratio increases. Figure 9b illustrates how the failure locus varies with

increasing temperatures and strain rates. The locus shifts toward higher failure strains for higher temperatures due to the temperature softening of the flow stress, while it shifts toward lower failure strains for higher strain rates due to strain rate hardening. This seemingly simple, one-parameter, failure criterion can thus account, at least qualitatively, for the varying stress-state, strain rate and temperature in complex ballistic impact problems, and it has been shown to predict the same trends as the five-parameter original JC failure criterion [37].

4.2 Model calibration

Table 3 presents the material parameters for the AR plates and the core of the 12 mm thick CH plates. To determine these, we conducted so-called inverse modeling, or reverse engineering, of the quasi-static tension tests. The simulation model was made in the IMPETUS Afea Solver using the same procedure as in Holmen et al. [18]. Since the solver uses explicit time integration we scaled the analysis time with a factor 10^{-4}. The kinetic energy was found to be negligible compared to the plastic dissipation of the model.

The procedure of determining the material parameters started by making a direct fit of the hardening rule (first term) in Eq. (3) to the equivalent stress-plastic strain curve determined by Bridgman's analysis. Then, sequential finite element simulations were conducted where the material parameters were varied to obtain a good fit to an experimental reference curve. In this case, the measured force-diameter reduction curve from the tension test was used in the optimization procedure. The optimized equivalent stress-plastic strain curves are shown in Figure 1. Last, to determine the CL failure parameter W_{cr}, the major principal stress was integrated over the equivalent plastic strain in the critical (i.e., central) element in the numerical model until the point where the experimental test failed. Here we used elements of approximately the same size as in the subsequent ballistic impact simulations. Temperature softening and rate sensitivity could not be determined from the quasi-static tension tests, so m and c were taken from the literature. An approximately linear degradation of strength with

temperature is commonly assumed for steels, so $m = 1.0$ was chosen to represent both the AR and CH plates. Since the strain-rate sensitivity parameter c seems to be related to the strength of the material [16], we selected two different values for the AR and CH plates. For the AR plates, $c = 0.016$ was taken from a recent study on structural S355 steel that exhibits pronounced strain rate sensitivity [38]. For high-strength materials, the strain-rate sensitivity is lower and we adopted a value of $c = 0.005$ for the CH plates since the scaled yield stress of these plates mainly varies from 600 MPa to 2000 MPa. This value is consistent with the investigations in Børvik et al. [16].

After identifying the material parameters of the core of the 12 mm thick plates we used the hardness measurements to distribute the material properties across the thickness of all the CH plates. There are numerous studies on the relationship between hardness and tensile properties in the literature (see e.g., Zhang et al. [39] for additional references). Most of them follow some sort of "factor three" relationship, meaning that the Vickers hardness (in MPa) is approximately three times as high as the stress (also in MPa). However, it is not always obvious for which stress measure this is valid. In materials without significant work hardening the Vickers hardness is reported to be three times the initial yield stress [40]. In materials that work harden, the Vickers hardness is reported to be three times the true stress at some value of true strain [21][39][41], or three times the ultimate engineering tensile stress (UTS) [39][40]. The tension tests presented in Section 2 show that NVE 36 steel work hardens considerably (Figure 1), so hereafter we assume that the Vickers hardness is proportional to the UTS. To summarize, the subsequent calibration procedure is based on the following assumptions:

(1) The work hardening does not change across the thickness of the plate. This can be partially defended by looking at the equivalent stress–plastic strain curves in Figure 1 where the slopes of the curves are similar for the AR and CH plates after some plastic straining, indicating that the case hardening does not significantly change the work

hardening. Additional justification can be found in Børvik et al. [16] where tension-test data from five different high-strength steels was presented. It was found that although the yield stresses varied from 605 MPa to 1711 MPa, the work hardening was comparable.

(2) The Vickers hardness is proportional to the UTS. We do not presume any specific proportionality factor in this study. However, the proportionality factors were 3.56 for the 12 mm AR plate and 3.58 for the core of the 12 mm CH plate, i.e., where we have both tensile data and hardness measurements.

(3) The CL failure parameter W_{cr} is constant across the thickness of the plate which seems reasonable since higher strength often means lower failure strains. This means that even with large differences in yield stress, the absorbed energy before failure remains fairly constant [16].

The material test program provided the complete stress-strain curve (Figure 1) and hardness (Figure 2a) of the core of the 12 mm CH plate. This information will be used as a basis to distribute the material parameters towards the surfaces of the 12 mm plate and across the entire thickness of the 6 mm and 4 mm thick plates where we do not have tensile data, but only know the hardness distribution. Based on assumptions (1) and (2) above, we can estimate the UTS as a function of the z-coordinate (thickness coordinate in the plate) for every plate-configuration. Considère's criterion is then used to determine the strain at necking. Assumption (1) above now makes us able to calculate the initial yield stress $A(z)$ that gives the correct UTS at the determined necking strain as a function of z. By assigning this varying $A(z)$ to the correct integration points we have accounted for the hardness profile by changing only the initial yield stress. If we now invoke assumption (3) it is clear from the CL criterion that high stresses require less strain to reach the failure criterion and, conversely, low stresses require high strains to reach the failure criterion. This ensures a less ductile behavior at the high-hardness portions of the plates. The procedure is described in detail in the following paragraph.

First, we use proportionality between Vickers hardness HV and UTS, and find that

$$s_u(z) = \frac{\mathrm{HV}(z)}{\overline{\mathrm{HV}}}\,\overline{s}_u \tag{7}$$

where z is the thickness coordinate, $s_u(z)$ is the UTS, and $\mathrm{HV}(z)$ is the Vickers hardness at point z in the plate. The measured UTS and Vickers hardness values from the core of the 12 mm plate are $\overline{s}_u$ and $\overline{\mathrm{HV}}$, respectively. We then apply Considère's necking criterion that relates the true stress at necking to the rate of work hardening. By assuming negligible elastic strains and a uniaxial stress state (the latter is true until necking), the following relation is valid at necking (i.e., $p(z) = p_u(z)$) in a tension test of the material at position z through the thickness of the plate

$$\frac{\mathrm{d}\sigma_{\mathrm{eq}}(z)}{\mathrm{d}p} = \sigma_{\mathrm{eq}}(z)\,. \tag{8}$$

At negligible strain rates and room temperature, Eq. (3) reduces to

$$\sigma_{\mathrm{eq}} = \mathrm{A} + \sum_{i=1}^{2} Q_i\left(1 - \exp\left(-C_i p\right)\right). \tag{9}$$

Furthermore, the relation between the equivalent stress σ_{eq} and the engineering stress s up until necking in the tension test is

$$\sigma_{\mathrm{eq}} = s\exp\left(p\right). \tag{10}$$

Using Eq. (9) to calculate the left-hand side of Eq. (8) and Eqs. (7) and (10) to calculate the right-hand side, we get

$$Q_1 C_1 \exp\left(-C_1 p_{\mathrm{u}}(z)\right) + Q_2 C_2 \exp\left(-C_2 p_{\mathrm{u}}(z)\right) - \frac{\mathrm{HV}(z)}{\overline{\mathrm{HV}}}\,\overline{s}_u \exp\left(p_{\mathrm{u}}(z)\right) = 0 \tag{11}$$

This equation is solved for the equivalent plastic strain at necking $p_{\mathrm{u}}(z)$ using e.g., Newton's method at every measuring point. When $p_{\mathrm{u}}(z)$ is determined, combination of Eqs. (9), (10) and (7) gives the initial yield stress $A(z)$ as

$$A(z) = \frac{\mathrm{HV}(z)}{\overline{\mathrm{HV}}} \bar{s}_{\mathrm{u}} \exp\left(p_{\mathrm{u}}(z)\right) - Q_1\left(1 - \exp\left(-C_1 p_{\mathrm{u}}(z)\right)\right) - Q_2\left(1 - \exp\left(-C_2 p_{\mathrm{u}}(z)\right)\right). \quad (12)$$

Figure 10 shows the distribution of the initial yield stress across the thickness of the target configurations. If we also consider the third assumption that was given above, it means that the only parameter that explicitly needs to be varied across the thickness of the plates is the initial yield stress. Due to the assumption of a constant fracture parameter W_{cr}, the failure strain will automatically be lower toward the surface of the plates where the strength is higher. There are, however, two issues that must be commented on in Figure 10. First, to compare, the scaled yield stress assuming proportionality between yield stress and hardness is plotted together with the scaled yield stress assuming proportionality between UTS and hardness. The values diverge, especially toward the surface, meaning that the scale factor is lower if we use yield stress than if we use the UTS. Second, it appears that the scaled yield stress for the core of the second 6 mm plate is unrealistically low. This is, however, due to the nature of the scaling process, where the UTS is proportional to the hardness and the work hardening is unchanged over the thickness, and the low Vickers hardness value for the core of the plate. The hardness in the core of this plate is significantly lower than in the reference plate. If we consider instead the flow stress at 2 % plastic strain, we find that it is nearly the same as for a comparable AR plate with approximately the same hardness.

We ran simulations of uniaxial tension tests with different initial yield stresses to illustrate the effects of the approach described above. Only the initial yield stress A was changed in the simulations. The CL parameter and the other hardening parameters are listed for the CH state in Table 3. The results are plotted in Figure 11 and they illustrate that a higher A indeed gives lower failure strains.

4.3 Finite element models

All the finite element simulations of the ballistic tests reported in the following were conducted with the 3D non-linear explicit code IMPETUS Afea Solver [25] on a NVIDIA Tesla Kepler K20c GPU.

Figure 12 shows a picture of the simulation model for a 2×6 mm plate configuration. In the impact zone we used 64-node hexahedral elements with element sides of 0.75 mm × 0.67 mm in the in-plane direction and 0.5 mm in the thickness direction. One symmetry plane was introduced in the model to save computational time without constraining the solution needlessly. Although we consider the plates to be in contact at the beginning of each test, a 0.01 mm gap was left between the plates in the layered configurations to avoid initial contact penetrations. A penalty-based node-to-surface contact algorithm and a Coulomb friction coefficient $\mu = 0.05$ were assumed between all the structural components [42][43]. By taking advantage of the localized nature of high-velocity ballistic impact we modeled only a 75 mm × 100 mm in-plane part, not the entire extension of the plate. Translational boundary conditions were applied to two of the boundary edges while the two remaining sides were unconstrained (similar to the tests). The bullet was given various initial velocities normal to the target plate. No initial pitch or yaw were considered. We modeled the steel core of the bullet as a rigid body while the behaviors of the lead cap and brass jacket were represented by the Johnson-Cook type material model (Eq. (3)) and the Cockcroft-Latham failure criterion (Eq. (5)) with material parameters taken from Børvik et al. [16]; note that the Young's modulus of the lead cap should be 10,000 MPa and not 1000 MPa as misprinted in Ref. [16]. How the initial yield stress varies across the thickness of the different CH configurations is illustrated in Figure 13. Failure was introduced into the numerical models by node splitting. When the damage indicator in an integration point reaches its limit, the algorithm splits the nearest node into two nodes and creates new element surfaces perpendicular to the direction of major

principal strain or stress. In this study we split the nodes perpendicular to the direction of the major principal strain because strain-based node splitting is less sensitive to numerical noise than stress-based node splitting [18]. Note that internal nodes in the 64-node hexahedral elements cannot be split.

Simulations were run with regular velocity intervals to identify the ballistic limit velocities for all the configurations. This resulted in six simulations per configuration in the AR state, and four or five simulations per configuration in the CH state, giving 31 simulations in total. Each simulation ran for between 4 h and 12 h depending on the termination time required to complete the perforation process.

Mesh sensitivity was briefly investigated. Doubling the element size that was reported above decreased the residual velocity significantly, while halving the element size gave virtually no change in the residual velocity. We therefore consider that the mesh has converged for our purpose of determining the ballistic limit velocity.

4.4 Simulation results and discussion

Table 2 and Figure 6b summarize the results from the numerical simulations. The scaling of the initial yield stress that was necessary due to the case-hardening procedure increased the predicted ballistic limit velocity substantially compared to the plates in the AR state. The simulations predicted a 30% increase of v_{bl} in the 12 mm and the 2×6 mm configuration, while they predicted an increase of almost 50% in the 3×4 mm configuration.

We further find that layering affects the predicted ballistic limit velocity negatively for the AR plates resulting in a minor discrepancy between the numerical and experimental results (Figure 7). Numerical predictions underestimated the ballistic limit velocities for all the configurations in the AR state. The deviation was 5.4% for the 12 mm plate, 8.8% for the 2×6 mm configuration, and 11.2% for the 3×4 mm configuration. Possible reasons for these conservative predictions relate to the assumptions that were made in the making of the

numerical models. The failure criterion was based on one single test, the strain-rate sensitivity was taken from the literature and the material softening was presumed to be linear with the temperature. Friction also plays a major role in simulation of ballistic impact and it still remains a challenging topic. Assuming a Coulomb frictional coefficient μ of 0.05 between all the surfaces in the model is a simplification of the complex sliding that occurs between the various materials. A higher friction coefficient will give higher ballistic limit velocities.

The correspondence between experiments and simulations is slightly better for CH plates than for AR plates, see Figure 7. The simulations underestimated the ballistic limit velocity for the 12 mm thick plate and the 2×6 mm configuration by 2.4% and 3.1%, respectively. The ballistic limit velocity of the 3×4 mm configuration was, on the other hand, overestimated by 7.4%. In the same way as for the AR plates, the strain-rate and temperature sensitivities of the model were not experimentally determined in this study, and it is unclear if the chosen combination gives conservative or non-conservative results. The friction coefficient was assumed to be the same in the CH configurations as in the AR configurations, which seems reasonable.

Section 4.2 presented the assumptions we made to be able to distribute the material properties across the thickness of the CH plates. These assumptions constitute an uncertainty in the numerical simulations and affect both the strength of the material and the point of failure. The simulations especially overestimated the capacity of the 3×4 mm CH configuration. A possible reason for this is that the average hardness is very high for this configuration. The average hardness of the 12 mm plate was 554 kg/mm^2 which is similar to the average hardness of 560 kg/mm^2 of the 2×6 mm configuration. The 3×4 mm configuration had a higher average hardness of 650 kg/mm^2. This suggests that the finite element simulations are more dependent on the strength of the material than the experiments, either because of the assumptions latent in the scaling procedure or because of shortcomings in the finite element modeling.

Despite the slight quantitative discrepancy between simulations and experiments, the qualitative results are acceptable and the trends are captured by the simulation models. Figure 14 illustrates how the simulation models predict the perforation process. By comparing Figure 14a to Figure 14c we find for the AR plates that the 3×4 mm configuration exhibits more dishing than the monolithic 12 mm plate. Figure 14b and Figure 14d show simulations of CH configurations. They appear to predict more fragmentation than their AR counterparts, suggesting a less ductile perforation mechanism. This was also seen in the experiments. Further, the brass jacket was peeled off earlier in the simulations of the CH plates compared to the AR plates in a similar way as in the tests.

We consider the predicted ballistic limit velocities that in the worst case deviated by 11.2% to be satisfactory, especially when taking into account the complexity of the problem at hand and the relative simplicity of the simulation models. The results are of similar accuracy as comparable previous numerical studies [14][16][17].

In a final attempt to isolate the effect of the hardness profile, we simulated impacts on the 12 mm thick plate where the initial yield stress was kept constant over the thickness. Three different constant hardness values were chosen: 352 kg/mm^2 (corresponding to the average hardness in the core of the CH plate), 554 kg/mm^2 (corresponding to the average hardness across the entire thickness of the CH plate), and 791 kg/mm^2 (corresponding to the maximum hardness toward the outer surfaces of the CH plate). We used an initial velocity v_i of 900 m/s. The residual velocity increased with the average hardness, as expected. More interestingly we found that the configuration with a constant hardness of 554 kg/mm^2 offered greater perforation resistance than simulation of the CH configuration from Section 4.3 with a hardness profile as shown in Figure 2a, but with the same average hardness. The residual velocities were 404 m/s and 570 m/s, respectively. This suggests that case hardening may not be the best way of increasing the capacity of plates subjected to ballistic impact.

5 Conclusions

This paper investigated, with experiments and simulations, the behavior of layered and case-hardened steel plates subjected to ballistic impacts by 7.62 mm AP bullets. Case hardening increased the ballistic limit velocity of the target plates by at least 20 %. Lamination, on the other hand, did not increase the ballistic limit velocity, even though the average hardness in some of the layered plates was significantly higher than in the monolithic plate. Lamination reduced the capacity of the case-hardened (CH) plates more than the capacity of the as-received (AR) plates. The reason for this is possibly that the softer AR plates experienced more global plastic deformation (dishing) for an increasing number of layers. This might have counteracted the expected decrease in capacity. CH plates in all lamination configurations experienced almost no global deformation, thus they did not benefit from the additional energy dissipation.

The case-hardening procedure did not give consistent hardness profiles in this study and the reason for this is unknown. However, this was accounted for in the calibration of the material models and thus included in the finite element simulations.

Numerical simulations of the ballistic impacts on the AR plates gave conservative results within approximately 11%. The results became less accurate for an increasing number of layers. A method of scaling the yield stress based upon hardness measurements was presented so that the variation of material properties in the CH plates could be included in the finite element models. Numerical simulations of ballistic impact on the CH plates gave conservative results within approximately 3% except for the 3×4 mm configuration where the ballistic limit velocity was overestimated by 7.4%. Thus, the numerical predictions for the CH plates were of comparable accuracy to those of the AR plates.

Acknowledgment

This work was supported financially by the Norwegian Defence Estates Agency. The authors are grateful to former MSc-students Erlend Orthe and Henrik Thorsen for their contribution to the experimental part of this work.

References

[1] Teng X, Dey S, Børvik T, Wierzbicki T. Protection performance of double-layered metal shields against projectile impact. Journal of Mechanics of Materials and Structures 2007; 2: 1309-1330.

[2] Ben-Dor G, Dubinsky A, Elperin T. Investigation and optimization of protective properties of metal multi-layered shields: A review. International Journal of Protective Structures 2012; 3: 275-291.

[3] Marom I, Bodner SR. Projectile perforation of multi-layered beams. International Journal of Mechanical Sciences 1979; 21: 489-504.

[4] Corran RSJ, Shadbolt PJ, Ruiz C. Impact loading of plates – an experimental investigation. International Journal of Impact Engineering 1983; 1: 3-22.

[5] Dey S, Børvik T, Teng X, Wierzbicki T, Hopperstad OS. On the ballistic resistance of double-layered steel plates: An experimental and numerical investigation. International Journal of Solids and Structures 2007; 44: 6701-6723.

[6] Teng X, Wierzbicki T, Huang M. Ballistic resistance of double-layered armor plates. International Journal of Impact Engineering 2008; 35: 870-884.

[7] Holmen JK, Hopperstad OS, Børvik T. Low-velocity impact on multi-layered dual-phase steel plates. International Journal of Impact Engineering 2015; 78: 161-177.

[8] Gupta NK, Madhu V. An experimental study impact of hard-core projectiles on single and layered plates. International Journal of Impact Engineering 1997; 19: 395-414.

[9] Gupta NK, Iqbal MA, Sekhon GS. Effect of projectile nose shape, impact velocity and target thickness on the deformation behavior of layered plates. International Journal of Impact Engineering 2008; 35: 37-60.

[10] Iqbal MA, Chakrabarti A, Beniwal S, Gupta NK. 3D numerical simulations of sharp nosed projectile impact on ductile targets. International Journal of Impact Engineering 2010; 37: 185-195.

[11] Iqbal MA, Gupta NK. Ballistic limit of single and layered aluminium plates. Strain 2011; 47: 205-219.

[12] Almohandes AA, Abdel-Kader MS, Eleiche AM. Experimental investigation of the ballistic resistance of steel-fiberglass reinforced polyester laminated plates. Composites Part B: Engineering 1996; 27: 447-458.

[13] Zukas JA, Scheffler DR. Impact effects in multilayered plates. International Journal of Impact Engineering 2001; 38: 3321-3328.

[14] Flores-Johnson EA, Saleh M, Edwards L. Ballistic performance of multi-layered metallic plates impacted by a 7.62-mm APM2 projectile. International Journal of Impact Engineering 2011; 38: 1022-1032.

[15] Deng Y, Zhang W, Cao Z. Experimental investigation on the ballistic resistance of monolithic and multi-layered plates against ogival-nosed rigid projectile impact. Materials and Design 2013; 44: 228-239.

[16] Børvik T, Clausen A, Dey S. Perforation resistance of five different high-strength steel plates subjected to small-arms projectiles. International Journal of Impact Engineering 2009; 36: 948-964.

[17] Holmen JK, Johnsen J, Jupp S, Hopperstad OS, Børvik T. Effects of heat treatment on the ballistic properties of AA6070 aluminium alloy. International Journal of Impact Engineering 2013; 57: 119-133.

[18] Holmen JK, Johnsen J, Hopperstad OS, Børvik T. Influence of fragmentation on the capacity of aluminum alloy plates subjected to ballistic impact. European Journal of Mechanics A/Solids 2016; 55: 221-233.

[19] Lou DC, Solberg JK, Børvik T. Surface strengthening using a self-protective diffusion paste and its application for ballistic protection of steel plates. Materials and Design 2009; 30: 3525-3536.

[20] Leslie WC. The Physical Metallurgy of Steels. Washington: Hemisphere Publishing Corporation; 1981.

[21] Dieter GE. Mechanical Metallurgy: SI Metric Edition. London: McGraw-Hill Book Company; 1988.

[22] Xu X-P, Needleman A. Numerical simulations of fast crack growth in brittle solids. Journal of the Mechanics and Physics of Solids 1994; 42: 1397-1434.

[23] Camacho GT, Ortiz M. Computational modeling of impact damage in brittle materials. International Journal of Solids and Structures 1996; 33: 2899-2938.

[24] Komori K. Simulation of shearing by node separation method. Computers and Structures 2001; 79: 197-207.

[25] IMPETUS Afea AS. IMPETUS Afea Solver [internet]. IMPETUS Afea AS; 2016-06-15, [cited 2016-06-15]. Available from: http://www.impetus-afea.com.

[26] Ruggiero A, Iannitti G, Testa G, Limido J, Lacome J-L, Olovsson L, Ferraro M, Bonora N. High strain rate fracture behavior of fused silica. Journal of Physics: Conference series 2014; 500: 1-4.

[27] Olovsson L, Limido J, Lacome J-L, Hanssen AG, Petit J. Modeling fragmentation with new higher order finite element technology and node splitting. In: Proceedings of the 11th International Conference on the Mechanical Behaviour of Materials under Dynamic Loading. 2015. 04050, pp. 1-6.

[28] Buberg TA. Case hardening of Hardox 450 steel for increased ballistic strength [master's thesis]. Trondheim, Norway: Department of Materials Science and Engineering, Norwegian University of Science and Technology (NTNU); 2011.

[29] Orthe E, Thorsen H. Ballistic perforation of surface hardened mild steel plates [master's thesis]. Trondheim, Norway: Structural Impact Laboratory (SIMLab), Norwegian University of Science and Technology (NTNU); 2014.

[30] Wikipedia contributors. Martensite [internet]. Wikipedia, The Free Encyclopedia; 2016-06-11, [cited 2016-07-26]. Available from: http://en.wikipedia.org/wiki/Martensite.

[31] Recht RF, Ipson TW. Ballistic perforation dynamics. Journal of Applied Mechanics 1963; 30: 384-390.

[32] Zukas JA (Editor). Impact Dynamics. 1st ed. New York: John Wiley & Sons, Inc.; 1982.

[33] Backman ME, Goldsmith W. The mechanics of penetration of projectiles into targets. International Journal of Engineering Science 1978; 16: 1-99.

[34] Johnson GR, Cook WH. A constitutive model and data for metals subjected to large strains, high strain rates and high temperatures. In: Proceedings of the 7th International Symposium on Ballistics. 1983, pp. 541-547.

[35] Børvik T, Hopperstad OS, Berstad T, Langseth M. A computational model of viscoplasticity and ductile damage for impact and penetration. European Journal of Mechanics A/Solids 2001; 20: 685-712.

[36] Cockcroft MG, Latham DJ. Ductility and the workability of metals. Journal of the Institute of Metals 1968; 38: 176-191.

[37] Johnson GR, Cook WH. Fracture characteristics of three metals subjected to various strains, strain rates, temperatures and pressures. Engineering Fracture Mechanics 1985; 21: 31-48.

[38] Grimsmo EL, Clausen AH, Aalberg A, Langseth M. A numerical study of beam-to-column joints subjected to impact. Engineering Structures 2016; 120: 103-115.

[39] Zhang P, Li SX, Zhang ZF. General relationship between strength and hardness. Materials Science and Engineering A 2011; 529: 62-73.

[40] François D, Pineau A, Zaoui A. Mechanical Behaviour of Materials. Volume 1: Micro- and Macroscopic Constitutive Behaviour. 2nd ed. Springer; 2012.

[41] Ashby MF, Jones DRH. Engineering Materials 1: An Introduction to their Properties and Applications. 1st ed. Oxford; Pergamon Press; 1980.

[42] Ravid M, Bodner SR. Dynamic perforation of viscoplastic plates by rigid projectiles. International Journal of Engineering Science 1983; 21: 577-591.

[43] Zukas JA (Editor). High Velocity Impact Dynamics. 1st ed. New York: John Wiley & Sons, Inc.; 1990.

Tables

Table 1: Chemical composition of the as-received NVE 36 steel plates based on the material certificates

	C	Si	Mn	S	P	Al	Nb	Cr	Ni	Cu	Mo	V	Ti
12 mm	0.15	0.35	1.50	0.010	0.007	0.044	0.037	0.019	0.019	0.044	0.001	0.002	0.002
6 mm	0.15	0.26	1.48	0.006	0.018	0.036	0.023	0.03	0.01	0.04	0.004	0.003	0.015
4 mm	0.15	0.26	1.48	0.006	0.018	0.036	0.023	0.03	0.01	0.04	0.004	0.003	0.015

Table 2: Ballistic limit velocities and the parameters of the Lambert-Jonas equation

		Experiments			**Simulations**		
		v_{bl} (m/s)	a	p	v_{bl} (m/s)	a	p
AR	12 mm	579	1.00	2.21	548	1.00	2.10
	2×6 mm	592	1.00	2.21	541	1.00	2.13
	3×4 mm	571	1.00	2.36	507	1.00	2.08
CH	12 mm	737	1.00	2.06	719	1.00	2.15
	2×6 mm	719	1.00	2.17	697	1.00	2.11
	3×4 mm	703	1.00	2.06	755	1.00	2.00

Table 3: Model parameters for the AR plates and the core of the 12 mm CH plate (note that A varies across the thickness of the CH plates)

	ρ (kg/m^3)	A (MPa)	Q_1 (MPa)	C_1	Q_2 (MPa)	C_2	W_{cr} (MPa)	$\dot{\varepsilon}_0$ (s^{-1})	c	C_p (J/kg K)	m	α (K^{-1})
AR	7850.0	333.1	236.3	16.5	416.5	1.2	848	5.0×10^{-4}	0.016	452	1.0	1.2×10^{-5}
CH	7850.0	535.8	381.8	68.7	394.4	1.9	925	5.0×10^{-4}	0.005	452	1.0	1.2×10^{-5}

Figures

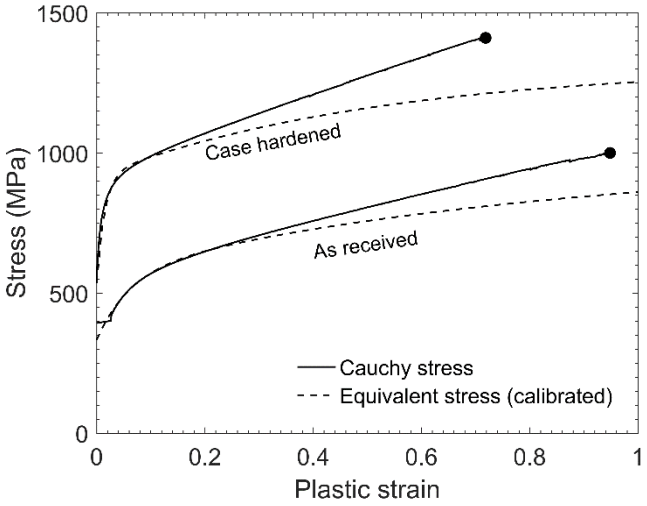

Figure 1: Cauchy (true) stress plotted against the plastic strain to failure in the tension tests, and the equivalent stress plotted against the equivalent plastic strain from the calibrated Voce hardening rule with values from Table 3

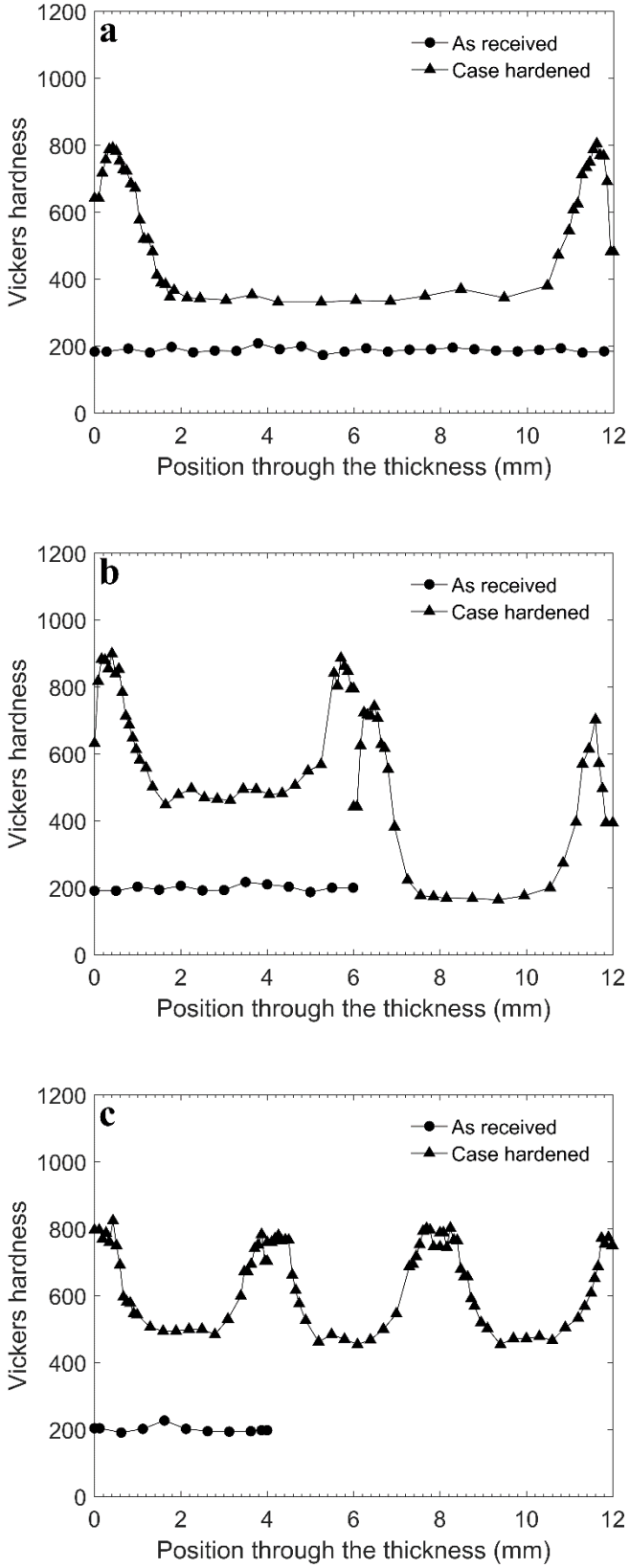

Figure 2: Results of the hardness measurements across the thickness of the target configurations. The Vickers hardness values are given in kg/mm^2: (a) 12 mm plate, (b) 2×6 mm plates, and (c) 3×4 mm plates. Only one of the 6 mm and 4 mm plates were measured to confirm that the hardness was approximately 200 kg/mm^2.

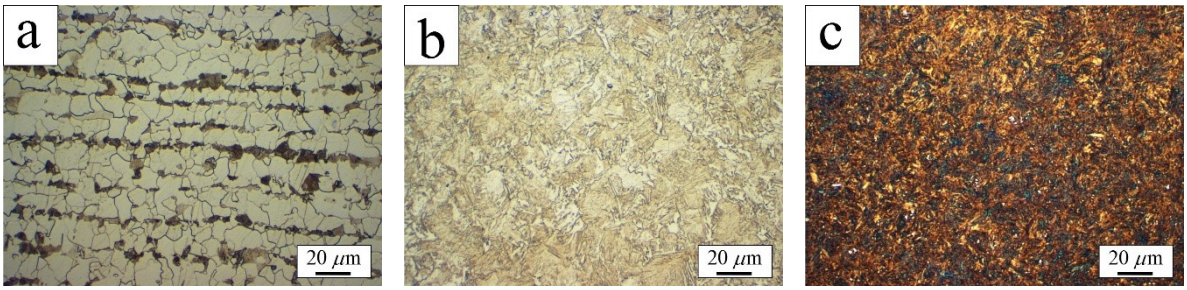

Figure 3: Micrographs of (a) ferrite/pearlite structure of the AR state, (b) martensitic structure of the core of the 12 mm plate, and (c) martensitic structure near the surface of the 12 mm plate.

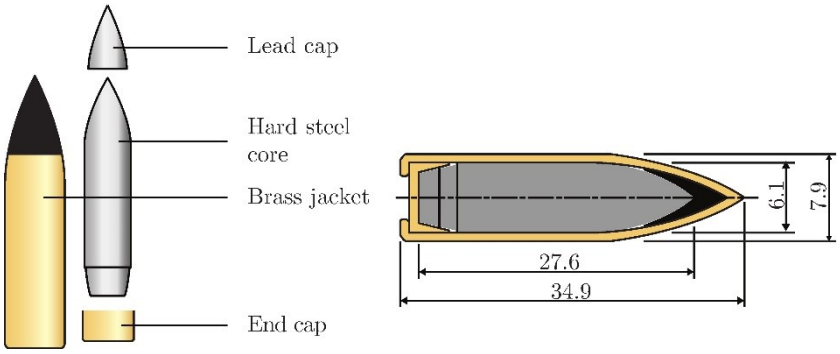

Figure 4: 7.62 mm armor piercing (AP) bullet. Measurements in mm.

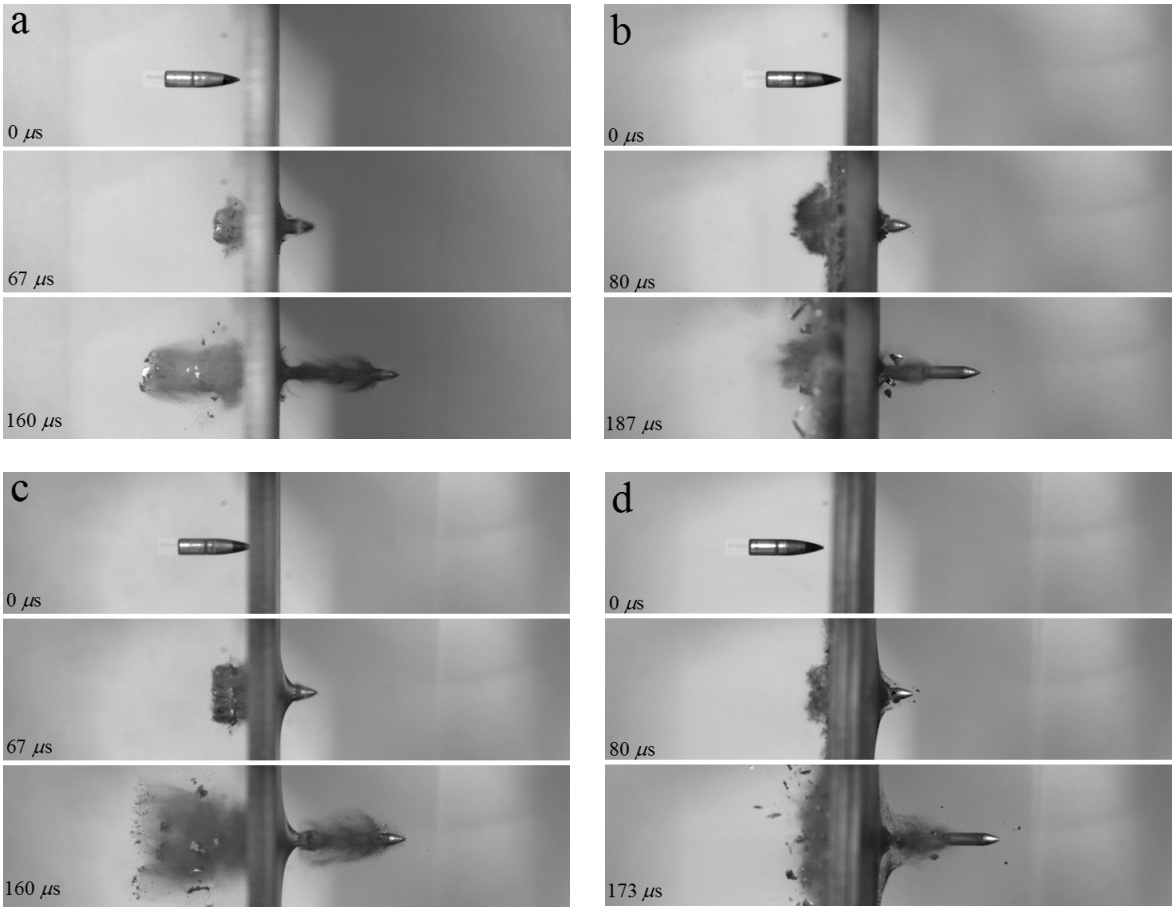

Figure 5: Some images from the perforation process: (a) AR 12 mm plate: v_i = 745 m/s, v_r = 501 m/s; (b) CH 12 mm plate: v_i = 789 m/s, v_r = 308 m/s; (c) AR 3×4 mm configuration: v_i = 703 m/s, v_r = 445 m/s; and (d) CH 3×4 mm configuration: v_i = 815 m/s, v_r = 392 m/s.

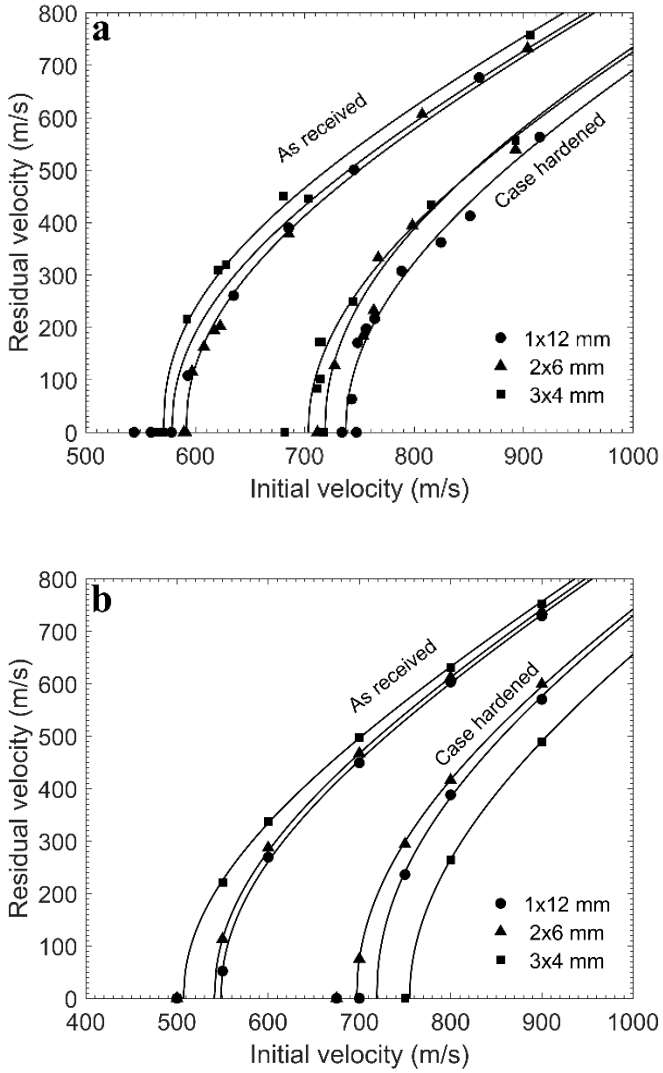

Figure 6: (a) Results from the experimental ballistic impact tests. (b) Results from the numerical simulations of the ballistic impact tests.

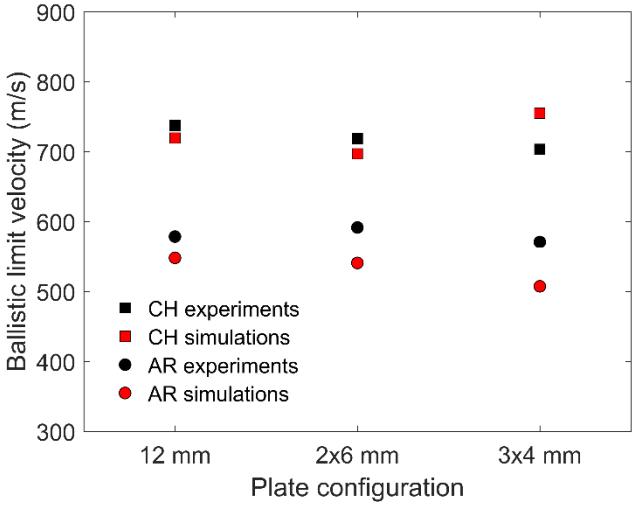

Figure 7: Ballistic limit velocity as a function of plate configuration for both experiments and simulations

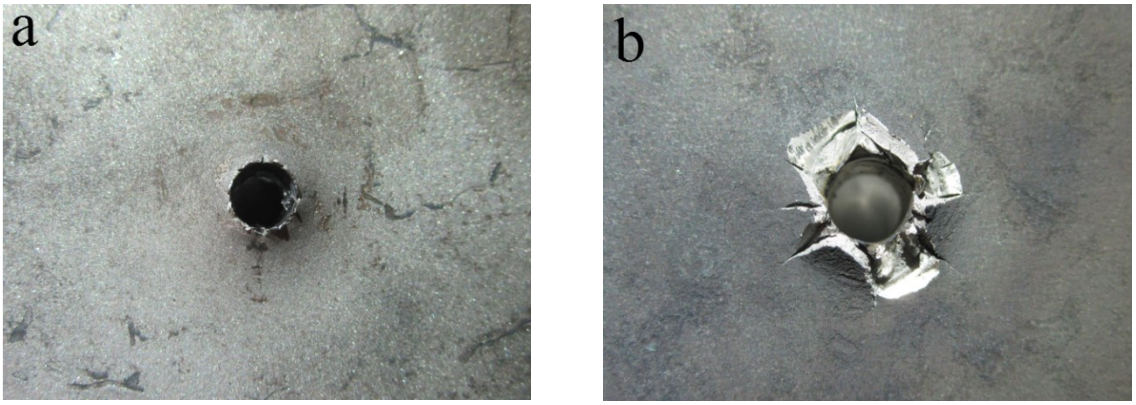

Figure 8: (a) Exit hole for impact on a 12 mm AR plate: v_i = 745 m/s, v_r = 501 m/s. (b) Exit hole for impact on a 12 mm CH plate: v_i = 789 m/s, v_r = 308 m/s.

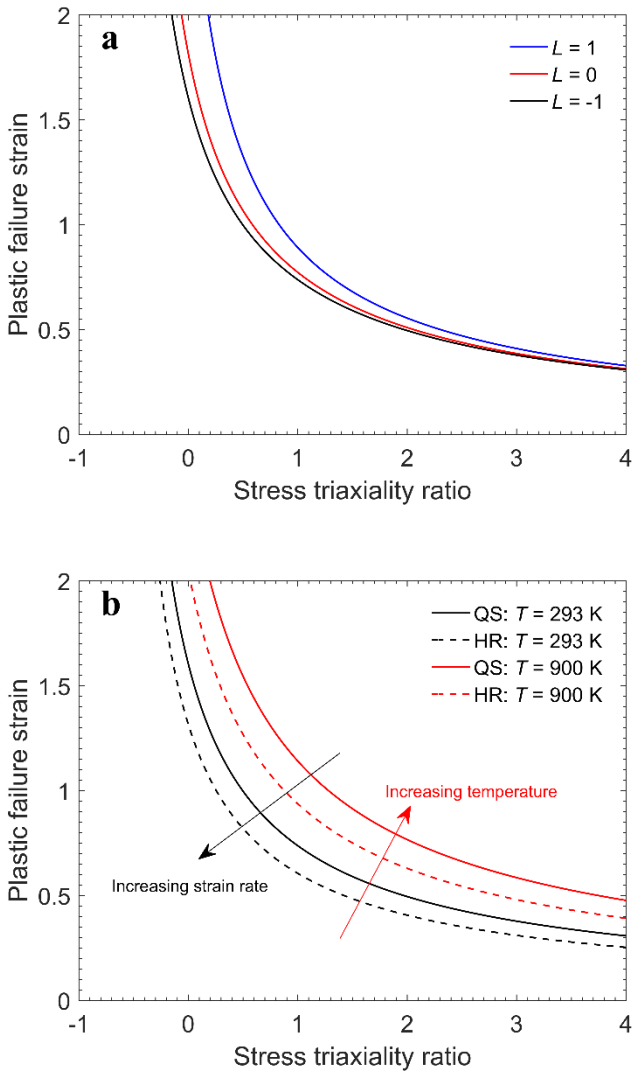

Figure 9: (a) Failure loci of the CL criterion showing its dependency upon stress triaxiality ratio and Lode parameter. (b) Failure loci for L = -1 showing how the failure strain varies with increasing temperature and strain rate. QS = quasi-static and HR = high rate (1000 1/s).

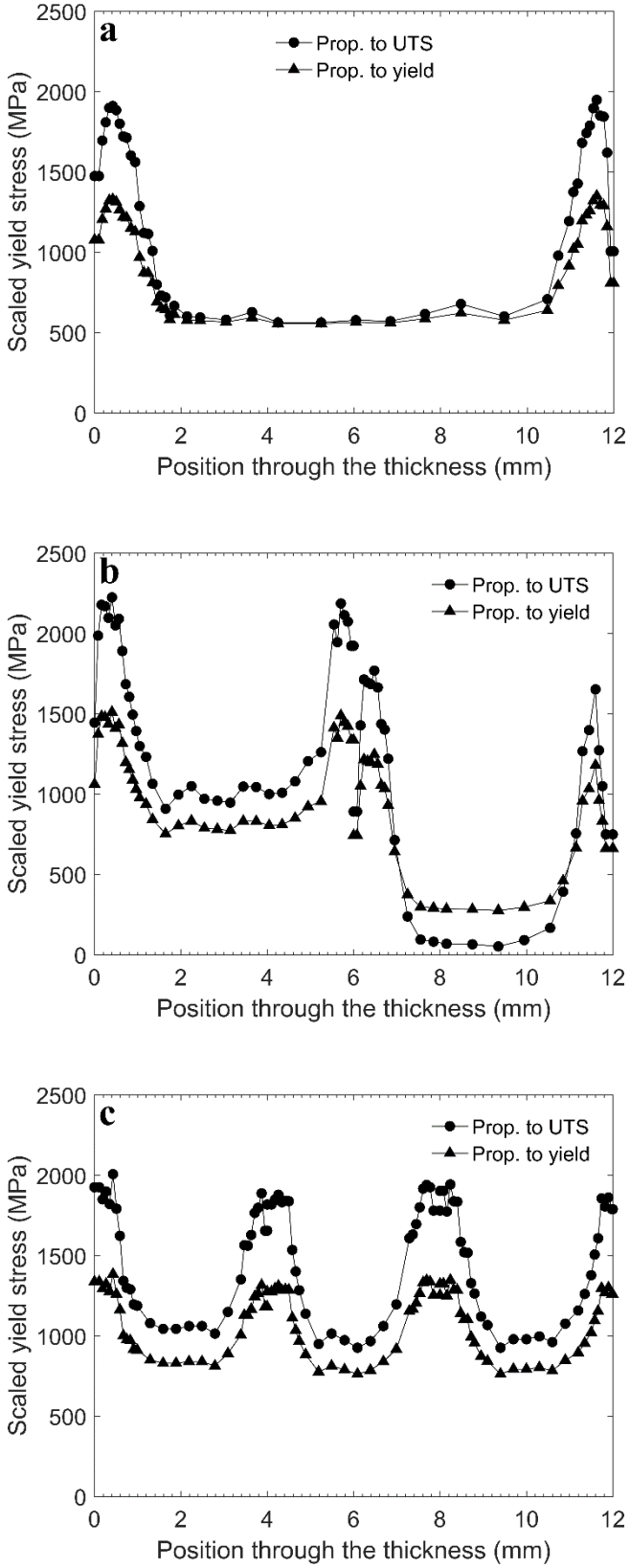

Figure 10: Scaled yield stress (A) across the thickness of the CH plates: (a) 12 mm plate, (b) 2×6 mm plates, and (c) 3×4 mm plates.

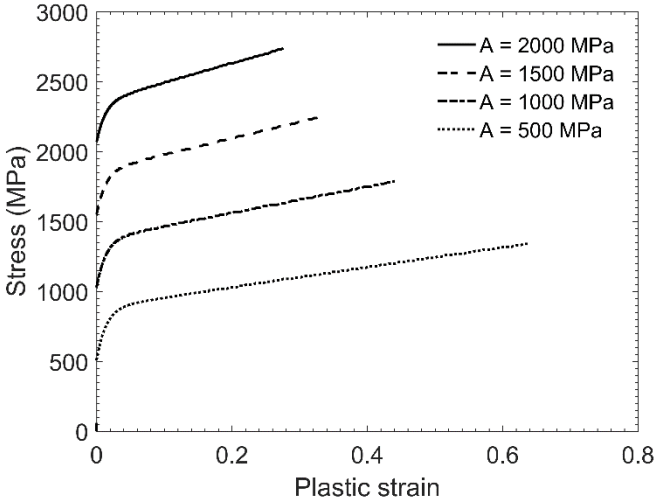

Figure 11: Cauchy (true) stress plotted against plastic strain from numerical simulations of tension specimens with various values of initial yield stress

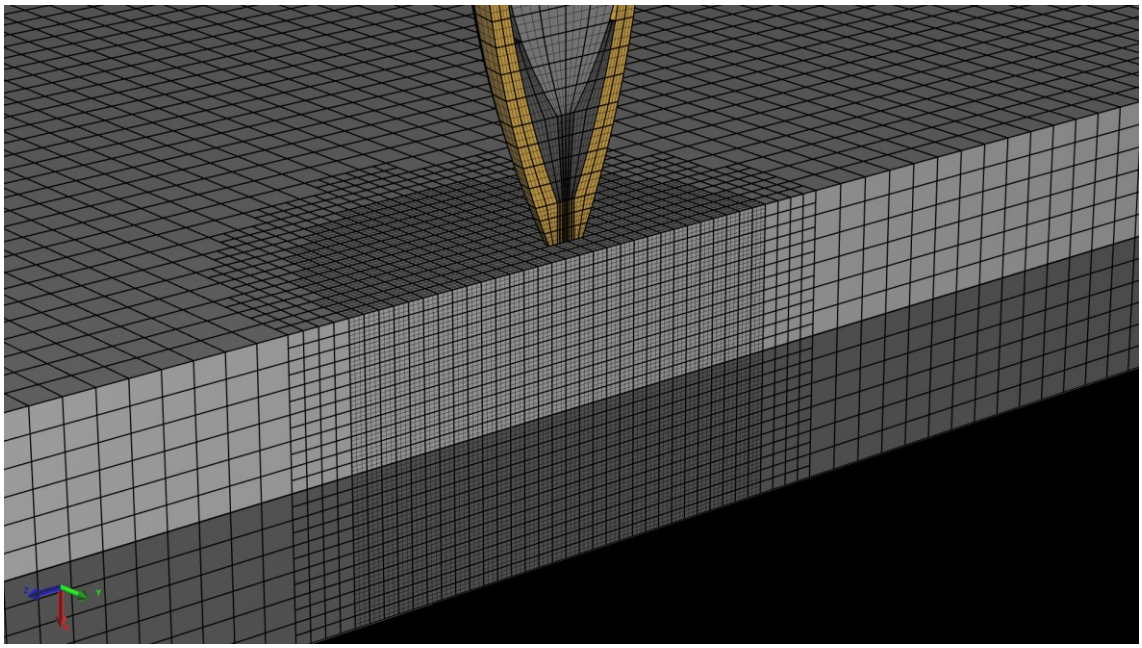

Figure 12: Picture of the initial simulation model of a 2×6 mm configuration before impact. The top and bottom plates are shown in different shades of gray.

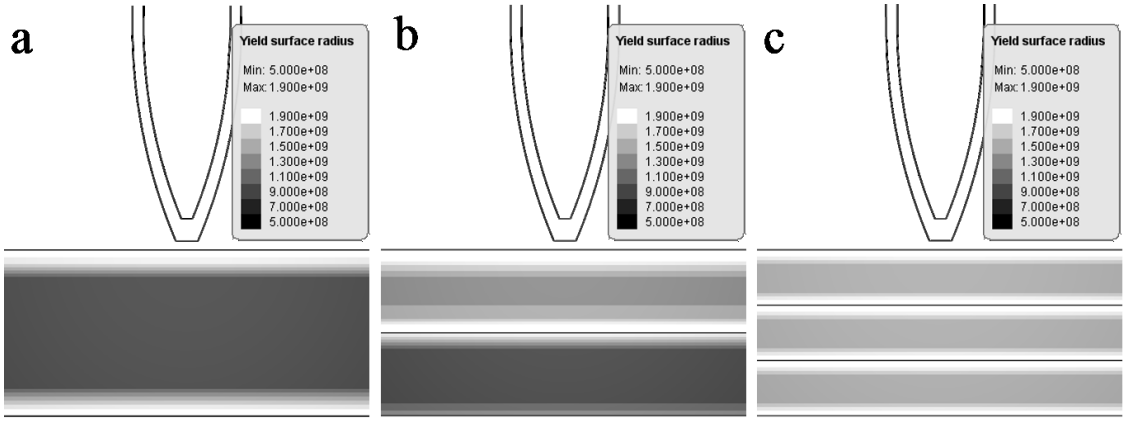

Figure 13: Distribution of the yield stress (in Pa) across the thickness of the three CH configurations: (a) 12 mm plate, (b) 2×6 mm plates, and (c) 3×4 mm plates.

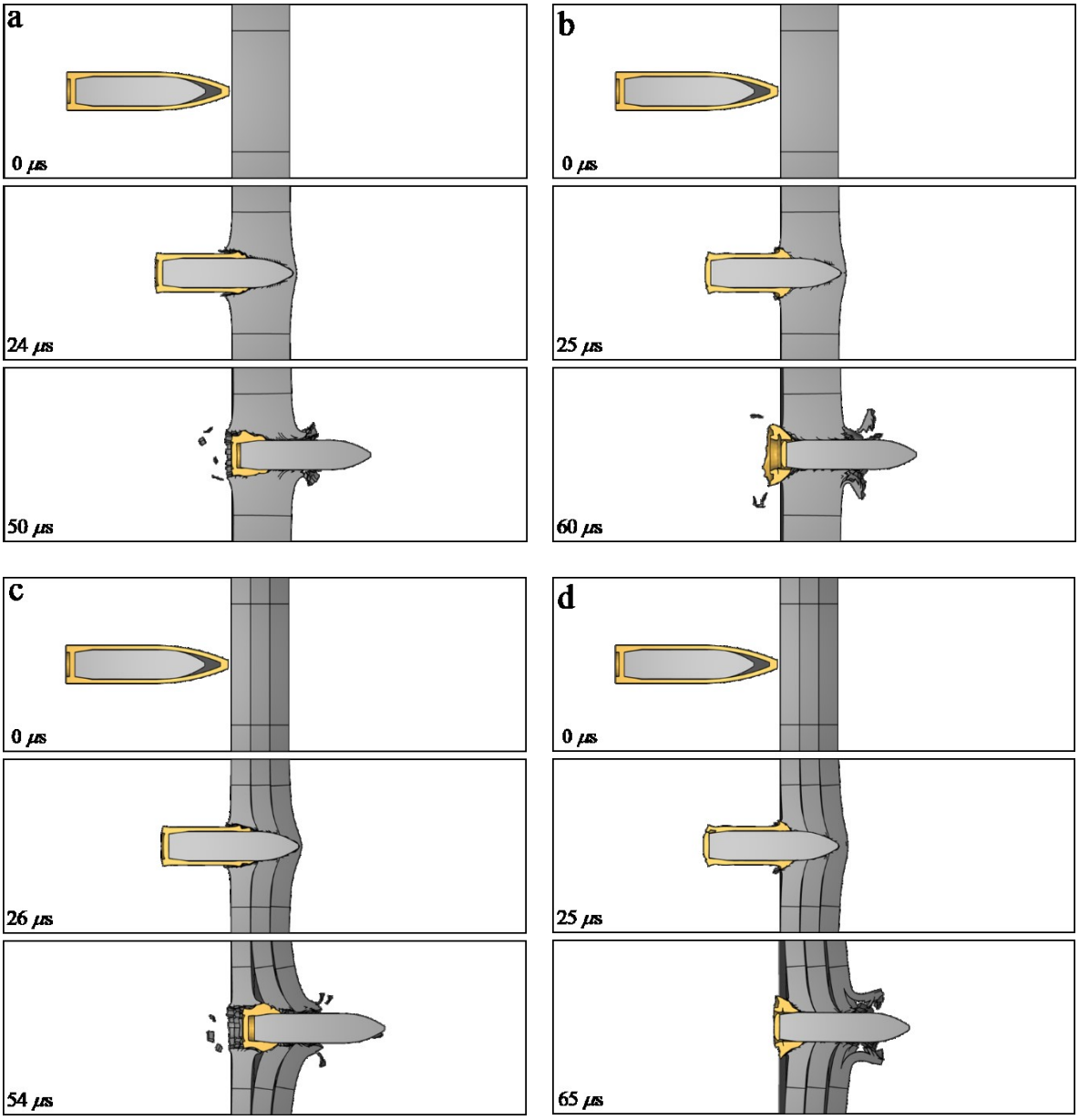

Figure 14: Images from the simulated perforation process. (a) AR 12 mm plate: v_i = 800 m/s, v_r = 603 m/s; (b) CH 12 mm plate: v_i = 800 m/s, v_r = 388 m/s; (c) AR 3×4 mm configuration: v_i = 800 m/s, v_r = 631 m/s; and (d) CH 3×4 mm configuration: v_i = 800 m/s, v_r = 264 m/s.